Electronic Supplementary Information

Construction of a wide-spectrum-responsive and high-activity photocatalyst, $Bi_{25}CoO_{40}$, via the creation of large external dipoles

Chengsi Pan[a,b]*, Zhenlin Wang[a,b], Yang Lou[a,b], Ying Zhang[a,b], Yuming Dong[a,b], Yongfa Zhu[a,b, c]

[a] Key Laboratory of Synthetic and Biological Colloids, Ministry of Education, School of Chemical and Material Engineering, Jiangnan University, Wuxi, Jiangsu, 214122, China

[b] International Joint Research Center for Photoresponsive Molecules and Materials, Jiangnan University, Wuxi, Jiangsu 214122, China

[c] Department of Chemistry, Tsinghua University, Beijing 100084, China

* To whom the manuscript should be contact: cspan@jiangnan.edu.cn

S1. Experimental Section

S1.1 DFT calculation

The electronic structures of $Bi_{25}CoO_{40}$ were calculated on Material Studio with a CASTEP program package.[1] A 2 × 1 × 1 supercell of $Bi_{25}CoO_{40}$ was employed for the Density Functional Theory (DFT) calculation. To simplify the calculation and also, based on our XRD refinement results, a homogeneous Co^{3+} and Bi^{5+} distribution with a ratio of 1 : 1 was applied to the tetrahedral site of our crystal model. The Generalized Gradient Approximation (GGA) with the parameterization of Perdew–Burke–Ernzerhof (PBE) was used for exchange-correlation functionals. A plane-wave basis with a kinetic energy cutoff of 380.0 eV and a Monkhorst-Pack grid with a 1×2×2 k-point mesh for the integration in the Brillouin zone were used. The geometry optimization convergence thresholds were set with the maximum force of 0.01 eV/Å; maximum stress tolerance of 0.02 GPa; and the maximum atomic displacement of 0.0005 Å. The electronic minimization parameter of the total energy/atom convergence tolerance was 5.0 $\times 10^{-6}$ eV. The calculations were done with designed nonlocal norm-conserving pseudopotentials. For better description of the d orbitals of transition metal, we also used a Hubbard U parameter for the 3d orbital of Co, which was set to 3 eV as reported.[2]

S.1.2 PEC Measurements

For all the PEC measurements, three-electrode system was employed for the test with the photocatalysts as a working electrode (0.5 cm × 1 cm), a platinum net as a counter electrode (1 cm × 1 cm), and a standard Ag/AgCl electrode ($E_{AgCl/Ag}$=0.210 V vs. NHE) as a reference electrode, respectively. During the test, no bias voltage is applied for the system. All the PEC

experiments were conducted using a CHI working station (Chenghua Inc., Shanghai, China) and in a 0.1 M aqueous Na_2SO_4 solution as the electrolyte.

For Mott-Schottky analysis, a sinusoidal voltage perturbation with an amplitude of 50 mV and a series of frequencies of 10, 100, 1000 Hz were superimposed on the applied potential (-0.1 V - 0.3 V). The typical 3-electrode configuration was used for the measurements. The potential difference between the flat band potential and conduction band is assumed to be 0.1 V for $Bi_{25}CoO_{40}$ and γ-Bi_2O_3, on the basis of the general trend in previous Bi_2O_3 based semiconductor.

S1.2 Bandgap calculation

The energy levels of the CBM and VBM for $Bi_{25}CoO_{40}$ and γ-Bi_2O_3 were estimated according to the method reported by Xu et al.[3] From the absolute electronegativity of the constituent atoms and the experimentally determined bandgap energies of the semiconductors, the band positions can be obtained via the following equations:

$$\mathrm{Ec} = (\chi(\mathrm{A})^{\mathrm{a}} \cdot \chi(\mathrm{B})^{\mathrm{b}} \cdot \chi(\mathrm{C})^{\mathrm{c}})^{1/(\mathrm{a+b+c})} - 1/2\ \mathrm{E_g} + \mathrm{E_0} \quad (1)$$

$$\mathrm{Ev} = \mathrm{Ec} + \mathrm{E_g} \quad (2)$$

Here, χ(A), χ(B) and χ(C) are the absolute electronegativity of the constituent atoms A, B, and C, respectively; E_C, E_V and Eg are the energy levels of CBM, VBM, and the bandgap energy of the semiconductor as determined by optical measurement, respectively; and E_0 is the scale factor relating the reference electrode redox level to the vacuum level (E_0 = -4.5 eV for a normal hydrogen electrode (NHE)).

S1.3. Fluorescence decay spectrum

The PL decay spectra were measured by using a Fluorescence lifetime spectrometer (Lifespec ll, Edinburgh) equipped with a pulse laser (EPL375). The signals were recorded by using the time-correlated single photon counting (TCSPC) method. The PL decay curves were fitted on a software (F980) provided by the instrument, and various τ values are tested to obtain a good fitness. The decay time of the photogenerated carriers are represented as $\bar{\tau}$, which can be calculated by the following equation:

$$\bar{\tau} = \frac{B_1\% \times \tau_1^2 + B_2\% \times \tau_2^2 + B_3\% \times \tau_3^2}{B_1\% \times \tau_1 + B_2\% \times \tau_2 + B_3\% \times \tau_3} \quad (3)$$

Where B_1 and B_2 and B_3 represent the amplitudes of the fast and slow components, τ_1 and τ_2 and τ_3 represent the time constants. The fitting parameters used for our curves are listed in Table S5.

S2. Figures and Tables

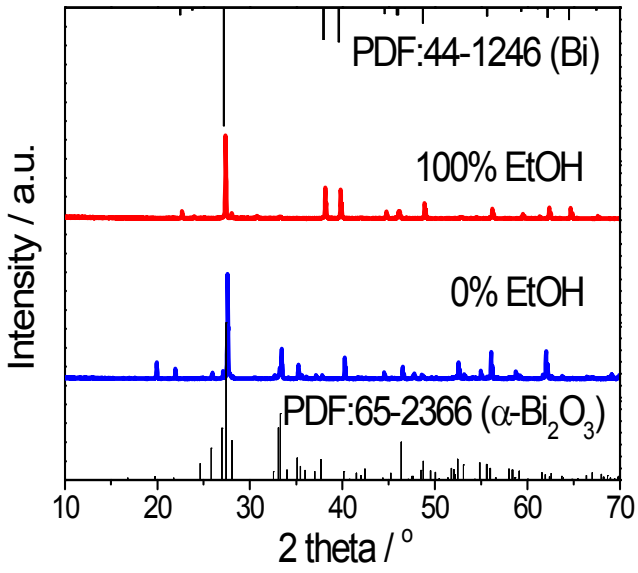

Figure S1. XRD patterns of the prepared samples with 0% and 100% EtOH added.

Figure S1 shows the XRD peaks of the control experiments with on EtOH addition and 100% EtOH as solvent. The peaks belong to monoclinic α-Bi_2O_3 (PDF No. 65-2366) with no EtOH addition and metallic Bi (PDF No. 44-1246) with 100% EtOH addition. The addition of EtOH facilitates the formation of sillenite phase, but at a risk of reduction of Bi^{3+}.

Table S1. XRD refinement parameters

Diffractometer	Bruker D8
Radiation	Cu Kα
Range	10-80°
Step	1°/min
Increment	0.02
Chemical formula	$Bi_{25.05}Co_{0.95}O_{40}$(ICP)
Space group	I23
Lattice constant	a=b=c=10.13653 (2) (A) α=β=γ=90°
Cell Volume (A^3)	1041.5
R_{wp}(%)	9.73
$\chi^2(R_{wp}/R_{ep})$	1.80
Atomic coordinates	Bi1 (0.1814(4) 0.3231(2) 0.4842(6)), Bi2 (0, 0, 0), Co (0, 0, 0), O1 (0.01579(5) 0.24835(3) 0.36434(2)), O2 (0.0938(1) 0.0938(6) 0.0938(4)), O3 (0.30317(3) 0.30317(8) 0.30317(5))
Occupation	Bi1 (0.999(2)), Bi2 (0.508(4)), Co (0.492(8)), O1 (0.999(3)), O2 (0.997(4)), O3 (0.995(5))

Isotropic Thermal Displacements Biso / Å^2	Bi1 (0.153(9)), Bi2 (0.165(2)), Co (0.781(4)), O1 (7.812(8)), O2 (7.212(7)), O3 (7.222(6))

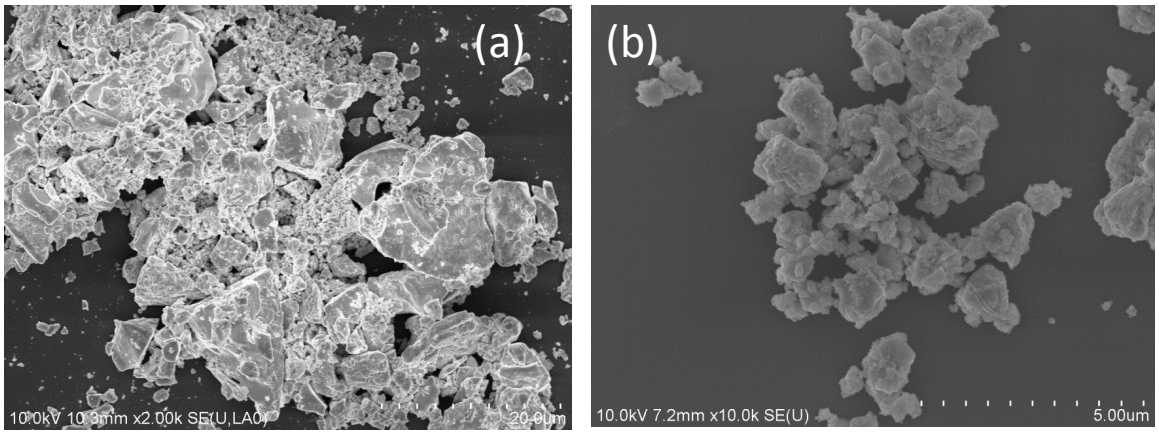

Figure S2. SEM images of $Bi_{25}CoO_{40}$ before (a) and after (b) ball milling.

The morphology of $Bi_{25}CoO_{40}$ before and after ball-milling treatment is shown in Figure S2. It is obvious that after ball milling, the big particles are broken and the secondary particle size becomes smaller than that before ball milling. But the primary particle size of the catalyst did not change significantly during the milling process.

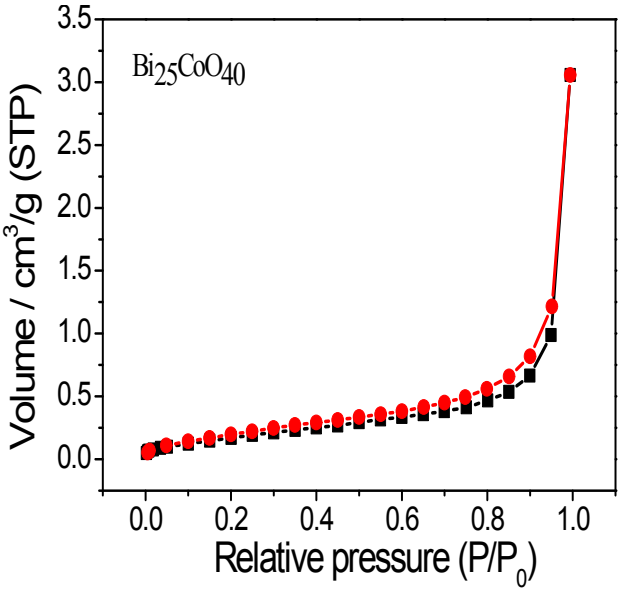

Figure S3. Isothermal adsorption-desorption curves of $Bi_{25}CoO_{40}$.

The ad-/desorption curves can be attributed to a type Ⅱ isotherm, indicating $Bi_{25}CoO_{40}$ has nonporous or macroporous characteristics.

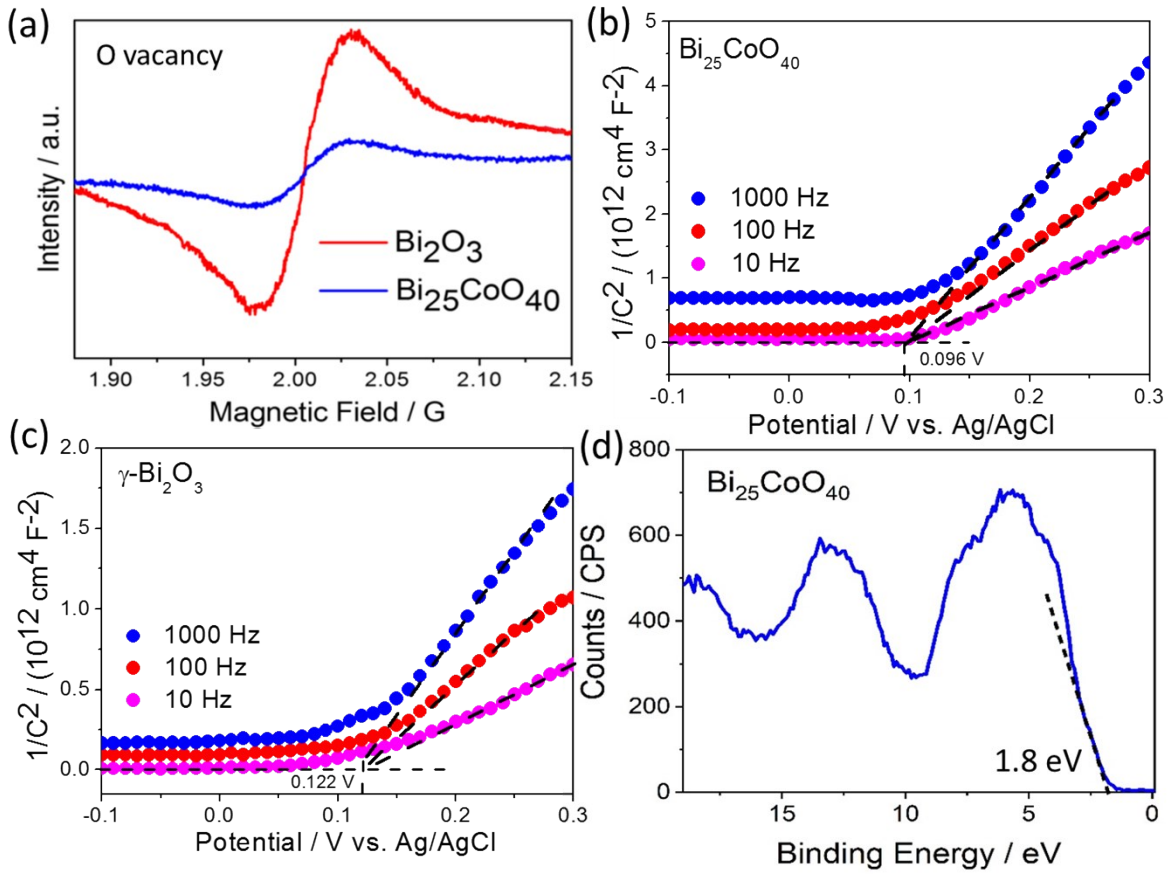

Figure S4 (a) EPR measurements for γ-Bi_2O_3 and $Bi_{25}CoO_{40}$ (room temperature, X-Band, Bruker EMXPLUS equipped dual cavity with modulation and microwave frequencies of 100 kHz and 9.846381 GHz, respectively). The signals are due to the existence of O vacancies in the structure. (b) and (c) Mott-Schotty curves of $Bi_{25}CoO_{40}$ and γ-Bi_2O_3 obtained at 10, 100, 1000 Hz in 0.1 M Na_2SO_4 aq (Ag/AgCl as the reference, Pt net as the counter). (d) XPS valence band spectrum of $Bi_{25}CoO_{40}$. 0 eV represents for the Femi level in the material.

Figure S4a shows the EPR measurements for γ-Bi_2O_3 and $Bi_{25}CoO_{40}$, respectively. The EPR signal occurs at g = ca. 2.001 for both γ-Bi_2O_3 and $Bi_{25}CoO_{40}$, which is an indicator of O vacancies originating from the Zeeman Effect of single electron trapped by oxygen vacancies. In the spectra, $Bi_{25}CoO_{40}$ shows one sixth intensity weaker than

that of γ-Bi_2O_3, indicating much less amount of oxygen vacancies exist in the $Bi_{25}CoO_{40}$ lattice.

The measured Mott-Schottky plots for are shown in Figure S4b and 4c. From these plots, the flat-band potentials (E_{fb}) of $Bi_{25}CoO_{40}$ and γ-Bi_2O_3 were found to be 0.096 V and 0.122 V vs. Ag/AgCl, respectively. Also, the curves confirmed that both the $Bi_{25}CoO_{40}$ and γ-Bi_2O_3 electrodes showed an anodic photoresponse, which indicated that they were n-type semiconductors. The conduction band minimum (CBM) was estimated according to the flat-band potential (E_{fb}) and the potential difference (ΔE) between CBM and flat-band potential.

$$E_{CBM} = E_{fb} - \Delta E \quad (4)$$

The XPS valence state spectrum was further measured for $Bi_{25}CoO_{40}$ to confirm the valence band edge as shown in Figure S4d. The spectra show that the VBM is 1.8 eV relative to the FEMI level. Since the flat band potential measurement shows that the FEMI level of $Bi_{25}CoO_{40}$ is 0.30 eV v.s. NHE, and thus the VBM is 2.1 eV, while the CBM is 0.4 eV.

Table S2. Performance comparison between our photocatalyst and the reported sillenite ones with visible-light response.

No.	Photocatalyst	Bandgap / ev	Degradation Performance	Ref.
1	$Bi_{25}CoO_{40}$	1.78 eV	6.4 mg/L MB, cat. 0.5 g/L, k = 3.402 h^{-1}, Xe lamp, λ > 420 nm 5 ppm 4-CP, cat. 0.5 g/L, k = 2.28 h^{-1}, Xe lamp, λ > 300 nm	This work
2	$Bi_{12}SiO_{20}$	2.46 eV	5 ppm RhB, cat. 0.4 g/L, k = 0.0533 h^{-1}, Xe lamp, λ > 420 nm	4
3	$Bi_{12}GeO_{20}$	2.30 eV	5 mg/L RhB, cat. 5 g/L, k = 0.094 h^{-1}, Dy lamp, λ>420 nm	5
4	$Bi_{25}VO_{40}$	2.31 eV	3.2mg/L MB, cat. 0.2 g/L, k = 0.094 h^{-1}, Xe lamp, λ > 420 nm	6
5	$Bi_{26-x}Mg_xO_{40}$	2.69 eV	100 ppm phenol, cat. 1 g/L, k = 0.394 h^{-1}, Xe lamp, λ > 420 nm	7
6	$Bi_{24}Al_2O_{39}$	2.6 eV	20 mg/L ARG, cat. 1g/L, k = 2.19 h^{-1}, Dy lamp, λ > 420 nm	8
7	$Bi_{12}TiO_{20}$	2.53 eV	10 mg/L RhB, cat. 1g/L, k = 1.194 h^{-1}, Hg lamp	9
8	$Bi_{24}O_{31}Br_{10}$	2.67 eV	40 mg/L RhB, cat. 1g/L, k = 1.194 h^{-1}, Hg lamp	10
9	$Bi_{12}TiO_{20}$ nanoflower	2.5 eV	10 mg PNP, cat. 1 g/L, k = 0.85 h^{-1}, 15 mg L^{-1} MO, cat. 1 g/L, k = 1.43 h^{-1}, Xe lamp λ > 320 nm	11
10	$Bi_{12}XO_{20}$, X = Si, Ge, Ti	2.5 - 2.9 eV	20 mg/L RhB, cat. 3 mg/L, k = 0.09 - 0.456 h^{-1}, Xe lamp λ > 320 nm	12
11	$Bi_{25}VO_{40}$	2.31 eV	10 mg/L MB, cat. 0.17 g/L, k = 0.58 h^{-1} Xe lamp λ > 420 nm	13
12	$Bi_{12}MnO_{20}$	1.86 eV	10 mg/L ARG, cat. 2 g/L, k = 0.76 h^{-1} 10 mg/L Cr(VI), cat. 1 g/L, k = 1.96 h^{-1} Dy lamp λ > 400 nm	14

Table S3. Performance comparison between our photocatalyst and the reported narrow bandgap photocatalysts with light adsorption > 700 nm.

No.	Photocatalyst	Bandgap / ev	Degradation Performance	Ref.
1	$Bi_{25}CoO_{40}$	1.78 eV	6.4 mg/L MB, cat. 0.5 g/L, k = 3.402 h^{-1}, Xe lamp, λ > 420 nm 5 ppm 4-CP, cat. 0.5 g/L, k = 2.28 h^{-1}, Xe lamp, λ > 300 nm	This work
2	BiOI microspheres	1.85 eV	25 mg/L phenol, cat. 1 g/L, k = 0.877 h^{-1}, Xe lamp, λ > 420 nm	15
3	FeS_2 Film	0.95 eV	5mg/L MB, K= 0.541h^{-1} 15mg/L phenol , k = 0.367 h^{-1}, Xe lamp, λ>420 nm	16
5	Sb_2S_3	1.64 eV	10-70mg/L MB, cat. 1 g/L, k = 0.547 h^{-1}, Xe lamp, λ > 400 nm	17
6	BiOI microspheres	1.81 eV	50 mg/L phenol, cat. 1g/L, k = 0.469 h^{-1}, Xe lamp, λ > 400 nm	18
7	Cu_2S	1.3 eV	100 mg/L phenol, cat. 1g/L, k = 1.164 h^{-1}, Xe lamp, λ > 420 nm	19
8	$Bi_8(CrO_4)O_{11}$	1.83 eV	10 mg/L phenol, cat. 0.5g/L, k = 7.927 h^{-1}, Xe lamp, AM 1.5 G	20
9	CuO nanowires Film	1.85 eV	20 mg/L MO, k = 0.768 h^{-1}, nature light	21
10	Cu_2O	1.72 eV	10 mg/L MO, cat. 0.5 mg/L, k = 0.72 h^{-1}, Xe lamp λ > 420 nm	22
11	$ZnFe_2O_4$	1.9 eV	10 mg/L MB, cat. 1 g/L, k = 0.26 h^{-1} natural sunlight	23
12	PDI	1.69 eV	10 mg/L phenol, cat. 0.5g/L, k = 0.195 h^{-1}, Xe lamp, λ > 420 nm	24

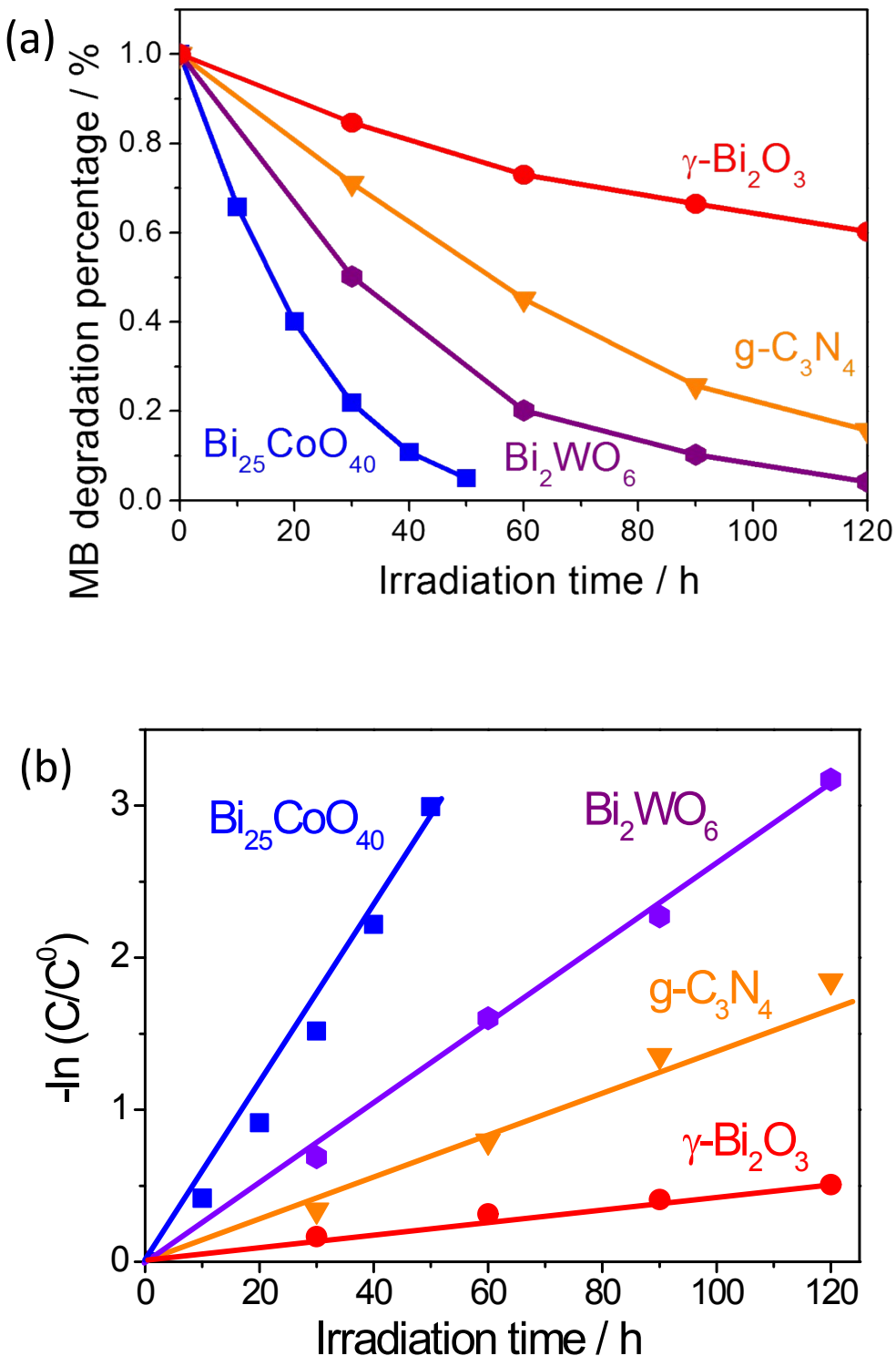

Figure S5. (a) Photodegradation curves of MB on $Bi_{25}CoO_{40}$, γ-Bi_2O_3, g-C_3N_4 and Bi_2WO_6 (b) Linear fitting for the concurrent photodegradation curves. 100 ml sln., $2*10^{-5}$ M MB, cat. 0.5 g/L, 300W Xe lamp equipped with a 420 nm cut-off filter.

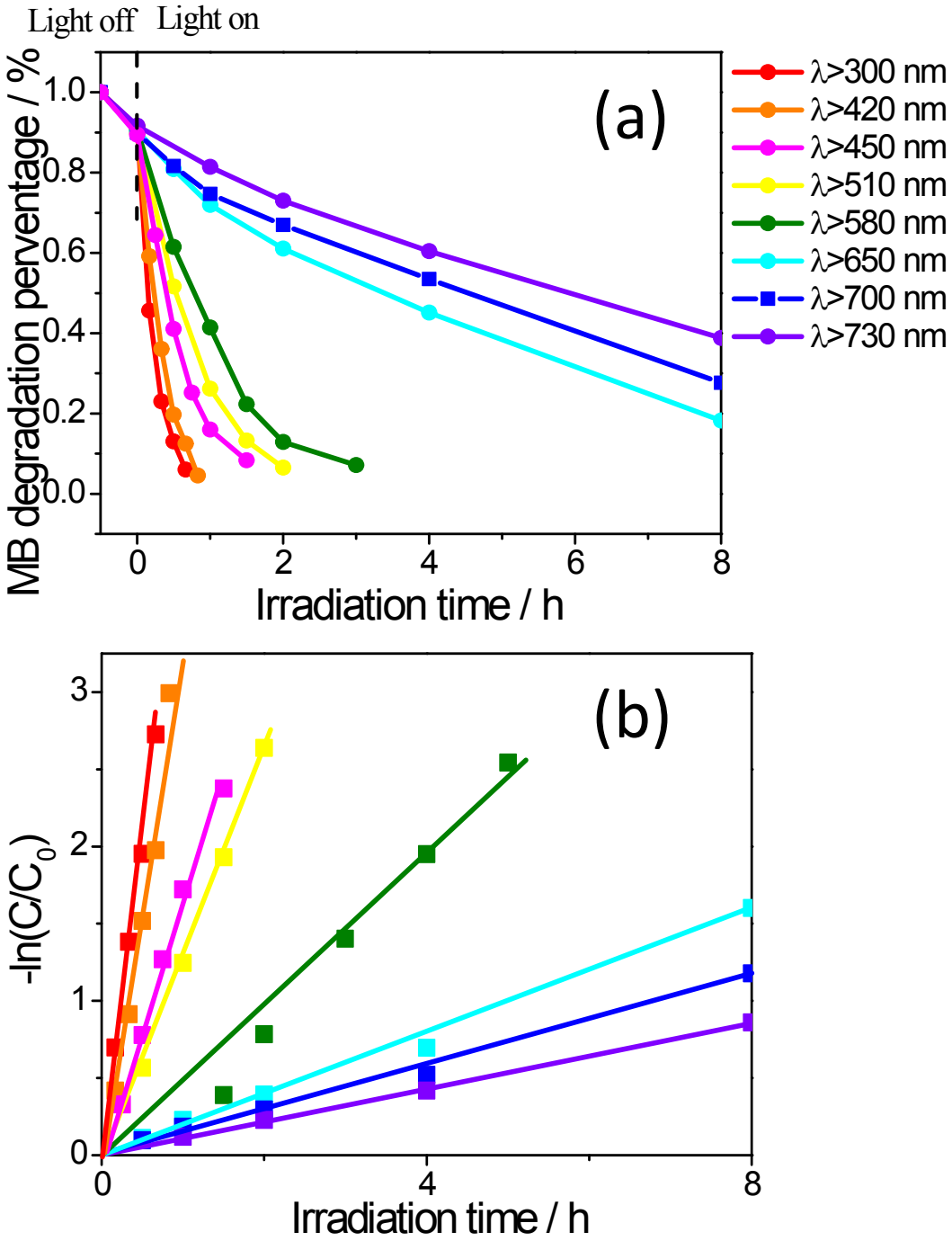

Figure S6. MB photodegradation on the sillenite $Bi_{25}CoO_{40}$ photocatalyst under different cutoff filters (a) and the concurrent linear fitting curves (b). 100 ml sln., $2*10^{-5}$ M MB, cat. 0.5 g/L, 300W Xe lamp equipped with various cut-off filters (300-730 nm)

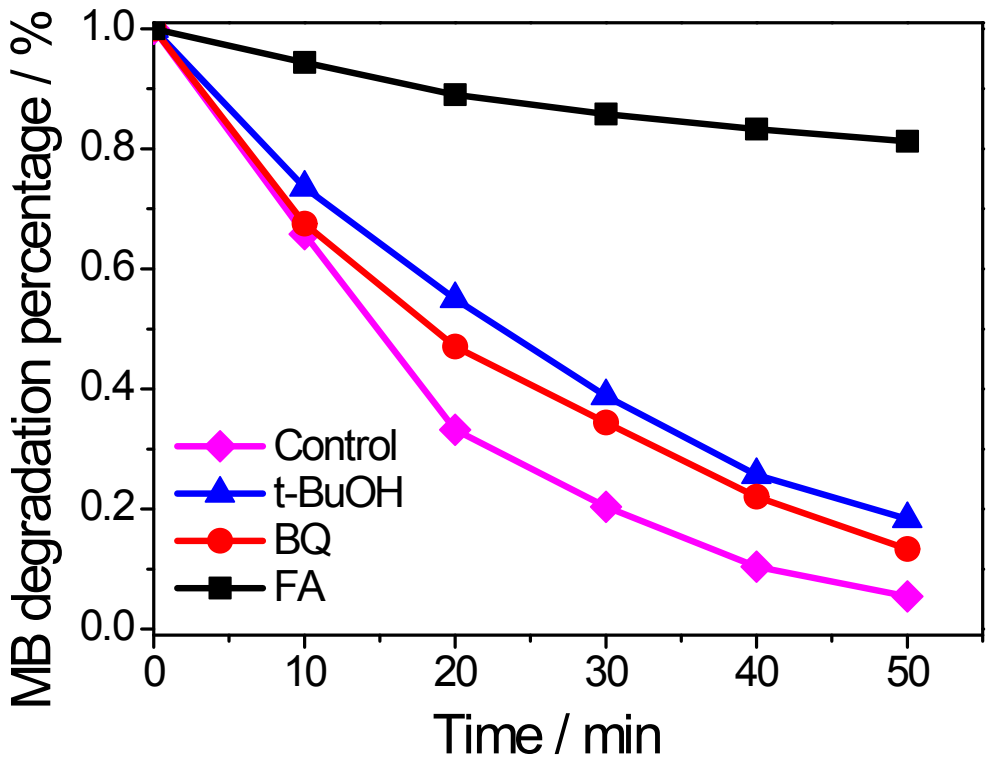

Figure S7. Active species capture during the MB degradation on sillenite $Bi_{25}CoO_{40}$. Control is the $Bi_{25}CoO_{40}$ photocatalyst without any capture reagent addition; t-BuOH is the capture reagent for hydroxide radicals; BQ is the capture reagent for super oxide radicals. FA is the capture reagent for holes.

Active species capturing experiments are shown in the Figure S7. It can be seen that FA can significantly decrease the degradation activity while t-BuOH and BQ show little influence on the activity. The results suggest that h^+ is the main active species in the process of MB degradation. This also supports the strong oxidation ability of the photocatalyst.

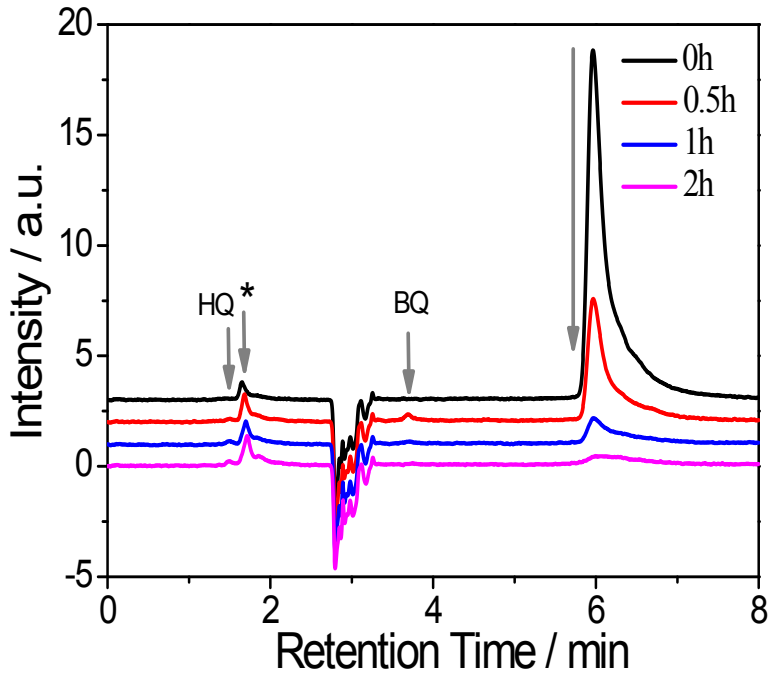

Figure S8. HPLC spectra of 4-CP degradation on $Bi_{25}CoO_{40}$. Benzoquinone (BQ) and hydroquinone (HQ) are the main degradation intermediates during the degradation process. The peak labeled with a star (*) is the impurities contained in the 4-CP. The BQ and HQ are determined by external standard.

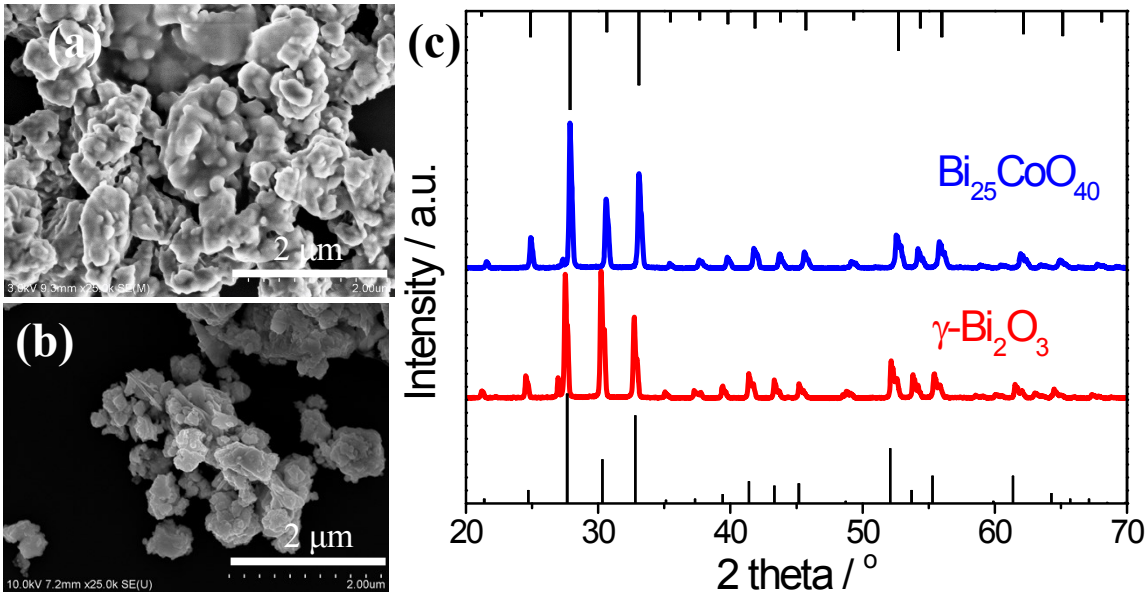

Figure S9. Structural comparison between $Bi_{25}CoO_{40}$ and γ-Bi_2O_3: SEM for (a) γ-Bi_2O_3 and (b) $Bi_{25}CoO_{40}$; (c) XRD for $Bi_{25}CoO_{40}$ and γ-Bi_2O_3

The morphology and X-ray diffraction results of the $Bi_{25}CoO_{40}$ and γ-Bi_2O_3 are shown in the figure S9. $Bi_{25}CoO_{40}$ and γ-Bi_2O_3 have no obvious difference in morphology, where γ-Bi_2O_3 shows a little higher agglomeration than $Bi_{25}CoO_{40}$. Also both $Bi_{25}CoO_{40}$ and γ-Bi_2O_3 belong to the cubic lattice, indicating by the X-ray diffraction results.

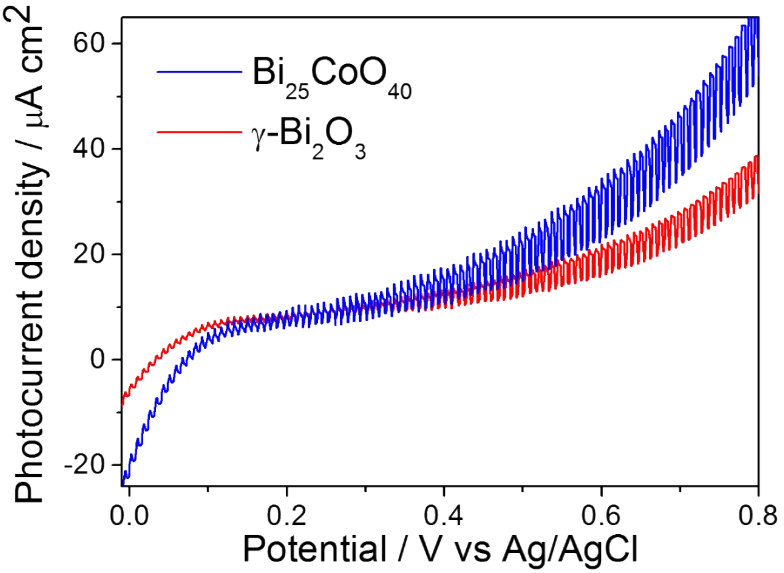

Figure S10. LSV curves for $Bi_{25}CoO_{40}$ and γ-Bi_2O_3, respectively. Three electrode system with a working electrode ($Bi_{25}CoO_{40}$ or γ-Bi_2O_3 on FTO), a platinum net as a counter electrode, and a standard Ag/AgCl electrode (E=0.210 V vs. NHE) as a reference electrode, respectively. Scan rate: 10 mV/s.

Table S4. Fitting parameters for EIS spectra

	R_s(Ω)	CPE ($Ssec^n$)	n	R_{ct} (kΩ)	Z_w ($Ssec^{0.5}$)
$Bi_{25}CoO_{40}$-in dark	33.7	89.7	0.721	66.3	5.2×10^{-4}
$Bi_{25}CoO_{40}$-light on	33.6	83.1	0.746	39.2	2.03×10^{-3}
γ-Bi_2O_3-in dark	40.2	65.1	0.75	29.3	6.09×10^{-4}
γ-Bi_2O_3-light on	41.1	89.2	0.76	6.12	9.4×10^{-3}

Table S5. Fluorescence spectrum fitting results

Sample	τ_1	τ_2	τ_1	B_1%	B_2%	B_3%	$\bar{\tau}$
$Bi_{25}CoO_{40}$	0.1288	0.8479	7.4137	0.914	0.0736	0.0124	2.76
γ-Bi_2O_3	0.0655	0.6793	/	0.7716	0.2284	/	0.53

References

1. S. J. Clark, M. D. Segall, C. J. Pickard, P. J. Hasnip, M. I. J. Probert, K. Refson and M. C. Payne, *Zeitschrift für Kristallographie - Crystalline Materials*, 2005, **220**, 567-570.
2. J. Janek, M. Martin and K. D. Becker, *Phys Chem Chem Phys*, 2009, **11**, 3010.
3. X. Yong and A. A. S. Martin, *American Mineralogist*, 2000, **85**, 543-556.
4. Q. Han, J. Zhang, X. Wang and J. Zhu, *Journal of Materials Chemistry A*, 2015, **3**, 7413-7421.
5. Z. Wan and G. Zhang, *Sci Rep*, 2014, **4**, 6298.
6. L.-C. Tien and I. C. Shen, *Materials Letters*, 2017, **202**, 73-77.
7. D. S. Shtarev, R. Kevorkyants, M. S. Molokeev and A. V. Shtareva, *Inorg Chem*, 2020, **59**, 8173-8183.
8. Z. Wan, G. Zhang, J. Wang and Y. Zhang, *RSC Advances*, 2013, **3**.
9. A. E. Nogueira, E. Longo, E. R. Leite and E. R. Camargo, *J Colloid Interface Sci*, 2014, **415**, 89-94.
10. J. Song, L. Zhang, J. Yang, X.-H. Huang and J.-S. Hu, *Materials & Design*, 2017, **123**, 128-136.
11. W. Guo, S. Zhang, Y. Guo, L. Ma, F. Su, Y. Guo and A. Geng, *RSC Advances*, 2013, **3**.
12. D. Hou, X. Hu, Y. Wen, B. Shan, P. Hu, X. Xiong, Y. Qiao and Y. Huang, *Phys Chem Chem Phys*, 2013, **15**, 20698-20705.
13. X. Qiao, Y. Pu, Y. Li, Y. Huang, H. Cheng and H. J. Seo, *Powder Technology*, 2016, **287**, 277-284.
14. X. Wu, M. Li, J. Li, G. Zhang and S. Yin, *Applied Catalysis B: Environmental*, 2017, **219**, 132-141.
15. X. Xiao and W.-D. Zhang, *Journal of Materials Chemistry*, 2010, **20**.
16. A. Tian, Q. Xu, X. Shi, H. Yang, X. Xue, J. You, X. Wang, C. Dong, X. Yan and H. Zhou, *RSC Advances*, 2015, **5**, 62724-62731.
17. J. Zhou, J. Chen, M. Tang, Y. Liu, X. Liu and H. Wang, *RSC Advances*, 2018, **8**, 18451-18455.
18. X. J. Wang, Y. Q. Song, J. Y. Hou and X. N. Chen, *Crystal Research and Technology*, 2017, **52**.
19. Y. Liu, Y. Deng, Z. Sun, J. Wei, G. Zheng, A. M. Asiri, S. B. Khan, M. M. Rahman and D. Zhao, *Small*, 2013, **9**, 2702-2708.
20. Y. Zhu, X. Ma, Y. Xu and X. Chen, *National Science Review*, 2020, **7**, 652-659.
21. X. Liu, Z. Li, Q. Zhang, F. Li and T. Kong, *Materials Letters*, 2012, **72**, 49-52.
22. H. Wang, Z. Lu, D. Lu, C. Li, P. Fang and D. Zhou, *Water Sci Technol*, 2016, **73**, 2379-2385.
23. N. G. Yadav, L. S. Chaudhary, P. A. Sakhare, T. D. Dongale, P. S. Patil and A. D. Sheikh, *J Colloid Interface Sci*, 2018, **527**, 289-297.
24. J. Wang, D. Liu, Y. Zhu, S. Zhou and S. Guan, *Applied Catalysis B: Environmental*, 2018, **231**, 251-261.